On the roles of liquid viscosity in droplet spreading at small Weber numbers

Zhenyu Zhang[a] and Peng Zhang[b*]

[a] School of Mechanical Engineering, Beijing Institute of Technology, Beijing, China.

[b] Department of Mechanical Engineering, The Hong Kong Polytechnic University, Kowloon, Hong Kong.

Abstract: Droplet impacting upon a free-slip plane at small Weber numbers ($We < 30$) was numerically investigated by using a front tracking method, with particular emphasis on clarifying the roles of the liquid viscosity and the "left-over" internal kinetic energy in droplet spreading. The most interesting discovery is that there exist a certain range of We, in which the maximum diameter rate $\tilde{D}_m$ shows a non-monotonic variation with the Reynolds number, Re. This non-monotonic variation is owing to the dual role of liquid viscosity in influencing droplet spreading. Specifically, when the initial surface energy is comparable to the initial kinetic energy (corresponding to We is around 10-30) , the high strain rates of the droplet internal flow dominates its viscous dissipation at relatively large Re, while the liquid viscosity dominates the viscous dissipation at relatively small Re. Furthermore, to unravel the influence of droplet attachment and detachment during droplet spreading, we considered two limiting situations such as full attachment (with no gas film throughout droplet spreading) and full detachment (with a gas film throughout droplet spreading). The results show that the droplet with a gas film tends to generate a stronger vortical motion in its rim, results in a larger left-over kinetic energy, and hence causes a smaller spreading.

Keywords: Droplet impact; maximum spreading diameter; gas film; viscosity; front tracking.

---

* Corresponding author
E-mail pengzhang.zhang@polyu.edu.hk.
Fax: (852)23654703 Tel: (852)27666664

The following publication Zhang, Z., & Zhang, P. (2019). Numerical interpretation to the roles of liquid viscosity in droplet spreading at small Weber numbers. Langmuir, 35(49), 16164-16171 is available at https://doi.org/10.1021/acs.langmuir.9b02736

1. Introduction

Liquid droplet impacting on a solid surface is relevant to many nature and industry processes, such as ink-jet printing [1], thermal spraying [2], self-clean surface [3], criminal investigation for police [4], and anti-icing for airplane wings [5]. In energy conversion devices such as combustion engines, the impact of fuel droplets on the intake port, cylinder liner, and combustion chamber may substantially influence subsequent combustion and emission performance.

Outcomes of droplet-wall impact such as spreading, splashing and bouncing are determined by the physical properties of liquid droplet, ambient gas, and solid surface. One of the most important quantities characterizing droplet-wall impact is the dimensionless droplet maximum spreading diameter $\tilde{D}_m = D_m/D_0$, where D_m is the droplet maximum spreading diameter and D_0 the initial droplet diameter. If the solid surface and ambient environment are fixed, $\tilde{D}_m$ are controlled by the Weber number, $We = \rho D_0 V_0^2/\sigma$, measuring the relative importance of droplet inertia compared to its surface tension, and the Reynolds number, $Re = \rho D_0 V_0/\mu$, characterizing the importance of the droplet viscosity with respect to the initial inertia, where ρ the liquid density, V_0 the droplet initial velocity, σ the liquid surface tension, and μ the viscosity. Sometimes, the Reynolds number can be replaced by the Ohnesorge number, $Oh = \mu/(\rho D_0 \sigma)^{1/2}$, measuring the ratio of viscous force over the surface tension force, because of the relation $Oh = \sqrt{We}/Re$.

A number of models have been proposed previously to predict $\tilde{D}_m$ in the past two decades, and majority of the models were established by fitting a large number of data under different conditions with various liquids or based on the scaling law [4, 6, 7, 8, 9, 10, 11], the force/momentum balance [12, 13], and the energy balance [10, 11, 14, 15, 16]. The momentum conservation approach predicts more accurate $\tilde{D}_m$ under relatively low viscosity conditions because viscous dissipation can be neglected. However, the energy conservation approach based models are more reliable when liquid viscosity must be taken into account.

In an energy conservation approach, quantifying the viscous dissipation during droplet spreading is crucial to accurately predict $\tilde{D}_m$. Inspired by the head loss theory in a pipe flow undergoing a sudden expansion [17], Wildeman et al. [16] proposed a “1/2-rule” indicating that approximately a half of the initial kinetic energy is transferred into surface energy for droplet impact on an ideal free-slip surface (with negligible surface friction) under $We \geq 30$; this “1/2-rule” also can be regarded as the head loss E_d^H. In the realistic non-slip condition, the additional viscous dissipation in the boundary layer E_d^{BL} should be added to the head loss to form the total viscous dissipation ($E_d = E_d^H + E_d^{BL}$). Good agreement was found between Wildeman et al.’s [16] model and the existing experiment results for a wide range of Re and for $We \geq 30$. However, large discrepancies exist for $We < 30$ because the “1/2-rule” breaks down.

To understand the ingeniousness and limitation of Wideman et al.’s model, we recognized that, at relatively high $We \geq 30$, the “pizza-like” droplet deformation becomes asymptotically accurate with increasing We and regardless of Re. In other words, the droplet internal flow is dominantly determined by We and almost independent of Re. Consequently, the liquid viscosity plays a “passive” role in affecting droplet spreading through modulating the viscous dissipation. For the free-slip case, the “1/2-rule” dominates the droplet spreading process, and liquid viscosity has a slight influence. For the non-slip case, the additional viscous dissipation within the boundary layer is linearly dependent on the liquid viscosity [16]. For smaller $We < 30$, the droplet deformation becomes more complex, undergoing a transition from being slightly deformed ($We < 1$) to being “puddle-shaped”($1 < We < 3$) and to being “pizza-shaped” ($3 < We < 30$). The absence of an asymptotic model for droplet deformation invalidates the “1/2-rule” and the “boundary-layer-like” flow assumption. Thus, it can be expected that there exists a more complex relation between viscous dissipation and spreading [12, 16, 18, 19], and that liquid viscosity may play an “active” role in substantially influencing droplet spreading along with We.

Previous works on the influence of liquid viscosity on droplet spreading were mostly focused on $We \geq 30$ and the results show that $\tilde{D}_m$ decreases monotonically with increasing viscosity. Recently, Qin et al. [20] experimentally investigated the droplet spreading on a smooth stainless steel surface at small We and observed a non-monotonic dependence of droplet spreading on liquid viscosity. Specifically $\tilde{D}_m$ first increases and then decreases with increasing liquid viscosity at two small Weber numbers ($We \approx 13$ and 30). Their interpretation to this observation is that, droplet deformation and the internal flow are not only controlled by impact inertia at small Wes but also by liquid viscosity. The reduction of flow strain rates by increasing viscosity could be more prominent than the increment of dissipation coefficient. Although this interpretation is qualitatively sound, it has not been validated by any experimental and numerical studies.

Another significant factor should be taken into account is the gas film between impacting droplet and solid surface. It has been well known that the air separating liquid droplet and solid surface must be drained out before the droplet contacts with the solid surface. If the air fails to be drained out and a gas film is therefore formed, the drop actually spreads out on the gas film. Under certain conditions, the spreading droplet may detach and reattach the surface to form a gas bubble [21]. Apparently, the existence of a gas film separating (entirely or partially) the liquid droplet interface from the solid surface substantially influences droplet spreading. Xu et al. [22] experimentally discovered that decreasing the ambient gas pressure suppresses droplet splashing. In addition, they observed a non-monotonic effect of viscosity on the splashing threshold pressures. Latka [23] and Kolinski et al. [24] experimentally found that viscosity effects are not important for droplet spreading and splashing with a gas film but are important if total wetting occurs upon contact with the surface, implying a gas film is absent.

Motived by the experimental observation of Qin et al. [20] and the numerical finding of Wildeman et al. [16], the present numerical study aims to understand the role of liquid viscosity in droplet spreading at small We. To consider the influence of a gas film but to avoid the complication of determining its formation, disappearance or topological change (bubble formation), we considered two simplified limiting situations, namely with and without a gas film throughout the spreading process. Another factor that complicates a numerical study is the characterization of surface, such as wettability, roughness and stiffness. To avoid the complication of characterizing various surface features and by following a similar approach of Wildeman et al. [16], we formulated the present problem as a droplet impacting on a free-slip surface (i.e. a symmetric plane). In spite of the above approximation and assumptions, we believe that the essential physics of viscosity effects in droplet spreading have been captured in the present problem.

2. Numerical methodology

To simulate the incompressible two-phase flow of a droplet impacting on a free-slip surface (a symmetrical plane), we adopted the Front tracking method (referred to as FTM hereinafter) that was developed by Tryggavason and his colleagues [25, 26, 27]. This FTM has been successfully used to simulate many multiphase problems including droplet dynamics [26, 28]. In the present simulation, an axisymmetric version of the unsteady Navier-Stokes equation is solved for both liquid and gas phases in a unified computational domain:

$$\frac{\partial(\rho \boldsymbol{V})}{\partial t} + \nabla\cdot(\rho\boldsymbol{V}\boldsymbol{V}) = -\nabla p + \nabla\cdot\mu[\nabla\boldsymbol{V} + (\nabla\boldsymbol{V})^T] - \sigma\int k\boldsymbol{n}\delta(\boldsymbol{x}-\boldsymbol{x}_f)dA \tag{1}$$

here, ρ, p, μ and σ are the density, pressure, viscosity, and surface tension, respectively. The vectors $\boldsymbol{V}$, $\boldsymbol{n}$, $\boldsymbol{x}$, are the velocity vector, a unit vector outwardly normal to the local surface, and the space vector. The subscript "f" denoting the gas-liquid interface. To account for the surface tension effects, a delta function integrated locally over the immiscible interface within unit volume is added into the equation. The governing equations are non-dimensionalized by the droplet initial velocity V_0, the liquid density ρ_l, and the droplet radius $R_0 = D_0/2$. Time is normalized by $T = {V_0 t}/{D_0}$, where t is the real time, D_0 the droplet initial diameter.

Figure 2 shows the computational domain of the present numerical simulation, a cylindrical coordinate $(r,\ z)$ is established so that the connection of the mass center for the droplets forms the radial direction, r, and the axial direction, z, is perpendicular to it. In the simulation, droplet is set to be with the non-dimensional impacting velocity correspond to the impacting Weber number. Axisymmetric boundary condition is specified for axis, while free-slip boundary conditions are specified to all the other boundaries including the impacting surface. The computational domain of $6 R_0$ in radius and $4R_0$ in height is discretized by a uniform orthogonal staggered mesh with 768×512 cells, which means each unit length contains 2^7 grid points. Grid-dependence analysis has been done and discussed in detail in our previous study [28], and will not be repeated here.

The present FTM has been sufficiently validated for binary collision of two equal-size droplets, which also can be regarded as a droplet impact on a symmetrical plane [12, 13, 16]. In Pan et al.'s [29] study, the predicted droplet profiles agree well with the experimental shadowgraphs with high temporal and spatial resolutions. This good agreement was subsequently reproduced by the authors[28, 30], in which Pan et al.'s [29] and Tang et al.'s [31] recent experimental results were used. Additionally, Qian and Law's [32] experimental results under various ambient pressures were also numerically reproduced by the present numerical method [30].

As discussed in the Introduction, we studied two limiting cases for droplet impacting on a free-slip surface, as shown in Figure 1. For case with a gas film in Figure 1(a), the gas film always exists and the droplet never contracts with the solid surface. By contrast, the other case without a gas film in Figure 1(b), the liquid droplet contacts the surface from the beginning and throughout the entire process of droplet spreading.

3. Results and discussion

3.1 Evolution of droplet deformation

It has been recognized that droplet spreading on a surface is a complex energy conversion process between kinetic energy and surface energy and with concomitant viscous dissipation. Previous studies always employed the Weber number as $We = \rho D_0 V_0^2/\sigma$ to represent the relative importance of droplet inertia compared with its surface tension. However, we found that this definition cannot precisely measure the relative importance of the initial kinetic energy and the surface energy. Consequently, In this study we proposed and advocated to use a revised Weber number $We_r = {}^{E_{k0}}/E_{s0} = \rho V_0^2 D_0/12\sigma = {}^{We}/12$, where the initial kinetic energy is $E_{k0} = \pi\rho V_0^2 D_0^3/12$ and the initial surface energy is $E_{s0} = \pi D_0^2 \sigma$. The advantage of using the new definition is to correctly reflect the orders of magnitude of various energies. For example, Wildeman et al.'s simulation found that the "pizza-like" droplet deformation becomes inaccurate for $We < 30$, which is equivalent to $We_r < 2.5$ in the new definition. Apparently, the latter is more physically reasonable in that the droplet deformation becomes less substantial when the initial energy and surface energy are of the same order, implying their ratio is of O(1).

Figure 3 shows the evolution of droplet deformation at three representative droplet Weber numbers ($We_r = 0.25$, 2.5 and 5.0) and various Ohnesorge numbers ($Oh = \sqrt{12We_r}/Re$). In each graph, droplet impacting with a gas film is shown on the left half while right half indicates droplet impacting without a gas film. Viscous dissipation rate (VDR) is also shown in the graphs.

For droplet impacting at relatively small inertia with $We_r = 0.25$, there is barely a difference of droplet shape with varied Ohs in the earlier stage at $T = 0.1$. The top of the droplet keeps its spherical shape and the bottom of the droplet contacts with the surface and substantially deforms. Notable viscous dissipation is observed near droplet rim, where large strain rate can be found. It is also observed that, with decreasing Oh, the viscous dissipation region moves from interior of the impacting droplet to the near surface region. Impacting droplet without a gas film produces significantly higher viscous dissipation rate, probably due to the larger spreading speed and hence strain rate. As droplet continues deforming after the earlier stage, liquid near impacting surface expends outwardly, and the droplet spreads gradually. A thick rim (when compared to D_0) was observed for either droplet impacting with a gas film or without a gas film at $T = 0.4$. At maximum spreading time instant τ_m, this thick rim becomes more prominent, and the droplet finally transform into a puddle-shaped droplet with a flattened top and a rounded edge for impacting with gas film case. However, for the impacting droplet without a gas film, it takes longer time to arrive at its maximum deformation and appears like a doughnut, and the droplet center height is significantly lower than that of rim.

For impacting droplet at intermediate inertia with $We_r = 2.5$, short after the early stage ($T = 0.4$), a thin rim is squeezed out from the bottom of the droplet and moves outwardly, and increasingly more liquid flows from center part of the droplet out into droplet rim and whirls around, as the results of the vertical flow motion in the rim at τ_m. The spreading droplet at τ_m can be regarded as a pizza-shaped droplet and contains two parts, namely, rim and lamella. Impacting droplet with a gas film show similar droplet deformation as that without a gas film case. With droplet impacting inertia increases to $We_r = 5.0$, the pizza shape becomes progressively more significant, and there is no distinct droplet shape can be observed. When compared to the impacting droplet with a gas film, that without a gas film produces relatively larger τ_m and maximum spreading diameter rate, because τ_m is proportional to $\tilde{D}_m$ and can be approximately estimated as $\tau_m = \tilde{D}_m - 1$ for $We_r > 2.5$ [16, 33].

3.2 "Monotonic – non-monotonic – monotonic" $\tilde{D}_m - Re$ transition at small We_r

Figure 4 shows $\tilde{D}_m$ for different We_r and *Re*s. From relatively small *Re* to relatively large *Re,* the corresponding Ohnesorge numbers $Oh = \sqrt{12We_r}/Re$ varies from 0.06 to 0.004, which corresponds to the glycerol droplets in Qin et al.'s [20] experiment. Overall, droplet impact on the solid surface with a gas film produces significantly smaller $\tilde{D}_m$ than that without a gas film, indicating the gas film actually suppresses droplet spreading, to be detailedly discussed in the following text.

Figure 4(a) shows the predicted $\tilde{D}_m$ for two limiting cases under various *Re*s at $We_r = 0.25$. In these cases where the initial kinetic energy is significantly smaller than the initial surface energy, $\tilde{D}_m$ increases rapidly and then increases slowly with *Re*. Similar result is also seen at $We_r = 1.0$, as shown in Figure 4(b). The monotonic increase of $\tilde{D}_m$ with Re is easily understandable as that the viscous dissipation decreases with increasing Re, and therefore more kinetic energy is converted into surface energy during droplet spreading.

An interesting phenomenon occurs at $We_r = 1.5$, as shown in Figure 4(c). For the cases without a gas film, $\tilde{D}_m$ still increases monotonically with Re. However, for the cases with a gas film, $\tilde{D}_m$ shows a non-monotonic trend with a peak value at around $Re = 638$. This non-monotonic variation of $\tilde{D}_m$ occurs for both the cases without a gas film and those with a gas film at $We_r = 2.0$, as shown in Figure 4(d), and at $We_r = 2.5$, as shown in Figure 4(e). It is also interesting to observe that, with We_r increases to 5.0, the non-monotonic trend disappears, and $\tilde{D}_m$ monotonically increases with Re as it was observed in previous studies concerning high impact Weber number.

The above "monotonic – non-monotonic – monotonic" $\tilde{D}_m - Re$ transition at small We_r is highly repeatable in the present numerical simulation and qualitatively consistent with Qin et al.'s [20] recent experimental results on the droplet spreading on a smooth solid surface at $We > 13$. They explained the "non-monotonic – monotonic" transition as that, at relatively small $We = 13$ and 30 (corresponding to $We_r \approx 1.0$ and 2.5), the droplet internal flow during spreading is strongly influenced by the viscous stress. Consequently, the viscous dissipation rate $\Phi = \mu f(\dot{\gamma})$ may be dominated by the liquid viscosity at relatively small Re while be dominated by the characteristic strain rate $\dot{\gamma} = g(We,\mu)$ at larger Re, which could be a monotonically decreasing function of liquid viscosity μ. The opposite trends with increasing μ results in the non-monotonic variation of $\tilde{D}_m$ with Re at relatively small We_r. The strain rate function becomes asymptotically independent of μ at higher We_r, rendering a monotonic variation of $\tilde{D}_m$ with Re. Although this explain is qualitatively sound, it was not sufficiently validated and the underlying energy conversion mechanism is to be clarified.

3.3 Energy budget at maximum droplet spreading

We show the energy budget at maximum droplet spreading for three representative cases (We_r = 0.25, 2.5 and 5.0), which respectively belongs to the monotonic, non-monotonic, and monotonic regimes, as shown in Figure 5. The kinetic energy E_k, surface energy E_s, and dissipated energy E_d were normalized by the initial kinetic energy E_{k0}. The surface energy change ΔE_s denotes the amount of kinetic energy transferred to the surface energy, and apparently we have $E_k + \Delta E_s + E_d = E_{k0}$.

At $We_r = 0.25$ shown in Figure 5(a), for the cases with a gas film, ΔE_s first increases from 0.6 at $Re = 29\ (Oh = 0.06)$ to around 0.7 at $Re = 104\ (Oh = 0.017)$ and then remains almost unchanged. This is because the energy budget is dominated by viscous dissipation at small *Re* but by surface energy when *Re* is sufficiently large. Similar tendency also can be found for the cases without a gas film, although less kinetic energy was transfer into surface energy and more kinetic energy is dissipated during droplet spreading.

The simulation results at $We_r = 2.5$ ($We = 30$) are shown in Figure 5(b). Previous studies [16, 20] found that for $We_r > 2.5$ ($We > 30$) the overall energy dissipation is approximately independent of We and Re. Wildeman et al. [16] subsequently proposed the "1/2-rule" that approximately a half of the initial kinetic energy transfers into the surface energy during droplet spreading, namely $\Delta E_s = 1/2$ in the present nomenclature. As seen in Figure 5(b), ΔE_s is however dependent on *Re,* and a non-monotonic tendency of ΔE_s is observed for the cases both with and without a gas film. This non-monotonic tendency is also seen for the cases without a gas film case at $We_r = 2.5$, as shown in Figure 5(c).

The non-monotonic tendency of ΔE_s is consistent with the non-monotonic variation of $\tilde{D}_m$ with *Re* shown in Figure 4. Liquid viscosity dominates the droplet internal flow at relatively small *Re*, while strain rate dominates the flow when Re is sufficiently large. Consequently, for droplet impact with an appropriate We_r, the maximum ΔE_s and the minimum E_d, as a result of competing viscosity and strain rate effects with increasing Re, cause a maximum $\tilde{D}_m$.

As droplet impact inertia increases to $We_r = 5.0$, ΔE_s increases first then arrives at a nearly constant value, agreeing well with the "1/2-rule" and with slight discrepancies among different *Re*s.

At relatively large *Re*s, droplet inertia dominates the energy budget, and the “pizza-like” droplet shape becomes gradually more pronounced, hence resulting in the similar viscous dissipation rate and E_d [12, 13, 16, 20]. For the cases without a gas film, slight discrepancies of ΔE_s from the “1/2-rule” can be observed, because a less amount of kinetic energy is transferred into the surface energy than being dissipated during droplet spreading.

3.4 Time evolutions of strain rate and viscous dissipation

To further unravel the underlying physics responsible for the non-monotonic tendency of E_d, we showed in Figure 6 the strain rate, viscous dissipation rate, and dissipated energy at $We_r = 2.5$. The time-dependent viscous dissipation rate is defined as $\Phi = \mu f(\dot{\boldsymbol{\gamma}})$, where $f(\dot{\boldsymbol{\gamma}})$ is given by

$$f(\dot{\boldsymbol{\gamma}}) = 2\left(\frac{\partial u}{\partial r}\right)^2 + 2\left(\frac{u}{r}\right)^2 + 2\left(\frac{\partial w}{\partial z}\right)^2 + \left(\frac{\partial u}{\partial z} + \frac{\partial w}{\partial r}\right)^2 - \frac{2}{3}\left[\frac{1}{r}\frac{\partial (ru)}{\partial r} + \frac{\partial w}{\partial z}\right]^2 \quad (2)$$

where, $\dot{\boldsymbol{\gamma}}$ is strain rate tensor, u is the velocity component in the *r*–direction, w the velocity component in z–direction.

As shown in Figure 6(a) and (b), the strain rate increases with *Re*. However, at relatively large *Re* ($Re = 1053$ and 782), we observed substantially higher strain rates than other *Re* by one order of magnitude. The viscous dissipation rate Φ is shown in Figure 6(c) and (d), on the left Y-axis. At relatively small Re, Φ increases with decreasing *Re*, indicating viscosity dominates viscous dissipation. At larger $Re = 1053$ and 782, Φ shows the same trend before about $T < 0.1$. However, after $T = 0.1$, the significantly higher Φ results in the higher E_d (on the right Y-axis) because of the substantially higher strain rate, indicating strain rate dominates Φ. After approximately $T = 0.3$, Φ decreases with increasing *Re*, indicating viscosity again dominates Φ.

3.5 Influence of gas film

We have seen in the previous sections that droplet impact with a gas film produces smaller $\tilde{D}_m$ than that without a gas film. To show the difference between two limiting conditions, we showed in Figure 7 the internal flow characteristics, such as stream line, vorticity and left-over kinetic energy at different Re and fixed $We_r = 2.5$. In the present axis-symmetric flow field, the vorticity vector has only one component in the azimuthal θ-direction:

$$\omega = \left(\frac{\partial u}{\partial z} - \frac{\partial w}{\partial r}\right) \tag{3}$$

where u is the velocity component in the r-direction and w the velocity component in the z-direction. The local left-over kinetic energy per unit volume is defined as $\frac{1}{2}\rho(u^2 + w^2)$. To show its distribution, we integrated the left-over kinetic energy as

$$E_k(r) = \int_0^{h_c(r)} \frac{1}{2}\rho(u^2 + w^2)dz \tag{4}$$

where $h_c(r)$ is the droplet height or the liquid film thickness at different r coordinates.

Overall, all predictions show similar droplet deformation (the "pizza-like" shape) and the spreading droplet can be divided into two parts, namely, rim and lamella. At relatively low $Re = 93$ ($Oh = 0.06$) shown in Figure 7(a), the dominant role of liquid viscosity in the energy budget results in that the majority of the kinetic energy was dissipated during droplet spreading, and that no apparent "ring-shaped" vortex is observed for both cases of with and without a gas film. A moderate extent of vorticity can be seen near the throttle between lamella and rim for the case with a gas film. Similar observation also can be made for the case without a gas film, which however has lower vorticity. $E_k(r)$ in the lamella is higher than that in the rim, indicating that the left-over kinetic energy mainly distributes in the droplet lamella rather than rim at relatively small Re. Compared with the case without a gas film, the case with a gas film possesses more left-over kinetic energy.

At Re=527($Oh = 0.01$) as shown in Figure 7(b), a significant "ring-shaped" vortex can be observed in both cases with and without a gas film, and it is responsible for the left-over kinetic energy discussed by Wildeman et al. [16]. Because the vorticity distributions in the rim and near the throttle are different, $E_k(r)$ in the rim is significantly higher than that in the lamella in the case with a gas film. However, in the case without a gas film, there is no significant difference of $E_k(r)$ between lamella and rim because of the relatively weak vertical motion in the rim.

As Re increases to 1053 ($Oh = 0.005$) as shown in Figure 7(c), we observed significantly intense vorticity and more left-over kinetic energy in the rim, indicating that increasing Re substantially promotes vortical motion in the rim and therefore increases the flow left-over kinetic energy. This explains the non-monotonic tendency shown in Figure 4 that, at relatively high Re, the droplet has more left-over kinetic energy stored in its rim, and therefore it has less initial kinetic energy for spreading.

4. Conclusion

A comprehensive numerical study on the droplet impact on a symmetrical plane with different impacting parameters is presented in this study, with particularly interesting in the droplet spreading at relatively small droplet inertias ($We_r < 2.5$ i.e., $We < 30$). The most interesting numerical observation is that, at relatively small droplet inertias ($We_r < 1.0$), the maximum spreading diameter ratio $\tilde{D}_m$ first increases then reaches a steady value with Re increasing. However, at intermediate Weber numbers (e.g. $We_r = 2.5$), $\tilde{D}_m$ first increases and then decreases with increasing Re, showing a non-monotonic variation with Re. This non-monotonic tendency disappears at higher droplet inertia (e.g. $We_r = 5.0$). These numerical findings are consistent with the recent experimental observations by Qin et al. [20].

By analyzing the numerical results on viscous dissipation, "left-over" internal kinetic energy, and vortical flow within the impacting droplet, a physical explanation to above "monotonic–non-monotonic–monotonic" $\tilde{D}_m$–Re transition has been obtained. For quite small droplet inertias, droplet deforms slightly from its spherical shape, and $\tilde{D}_m$ increases monotonically with Re increasing because viscous dissipation decreases with increasing Re (or decreasing Oh). For intermediate droplet inertias, droplet deformation and internal flow are not dominated by impact inertia. With increasing Re (or decreasing Oh) viscous dissipation rate is first dominated by liquid viscosity, and then the increase of internal flow strain rate becomes more prominent than the effect by decreasing the liquid viscosity, rendering an non-monotonic tendency of dissipation energy E_d with Re hence a non-monotonic $\tilde{D}_m - Re$ relation. As droplet inertia further increases, droplet deformations are increasingly controlled by the droplet inertia, and $\tilde{D}_m$ first increases rapidly and then slowly with increasing Re, as observed by many previous studies.

Previous studies often make an assumption that there is negligible internal motion within the droplet at maximum spreading. However, we observed substantial and varying internal flow at the maximum spreading, resulting in a significant amount of left-over kinetic energy that must be considered in energy budget. The energy can exist in two forms, such as the flow motion entering from lamella into the rim and the vortical flow in the rim.

Two limiting cases that droplet impacting with a gas film and without a gas film were considered in the present simulation. When compared to impacting droplet with gas a film, droplet spreading with a gas film produces stronger vortical flow in the rim, which contains more left-over kinetic energy, and hence causes a smaller spreading. Although these two cases are physically idealistic, they provide useful information about the role of gas film in affecting droplet spreading on a real solid surface, on which the gas film dynamics is far more complex and mertis future studies. More importantly, the present results on non-monotonic droplet spreading were found for both limiting cases, indicating the essential roles of liquid viscosity are correctly captured by the study.

Acknowledgement

This work at Beijing Institute of Technology was supported by the National Natural Science Foundation of China (grant no. 51806013) and Beijing Institute of Technology Research Fund Program for Young Scholars (grant no. 2019CX04031). The work at the Hong Kong Polytechnic University was supported by the Hong Kong Research Grants Council/ General Research Fund (PolyU 152217/14E and PolyU 152651/16E) and partly by Central Research Grant (G-SB1Q).

References

1. van Dam, D. B.; Le Clerc, C. Experimental study of the impact of an ink-jet printed droplet on a solid substrate. *Phys. Fluids* **2004,** *16* (9), 3403-3414.
2. Kim, J. H. Spray cooling heat transfer: The state of the art. *Int. J. Heat Fluid Flow* **2007,** *28* (4), 753-767.
3. Blossey, R. Self-cleaning surfaces - virtual realities. *Nat. Mater.* **2003,** *2* (5), 301-306.
4. Laan, N.; de Bruin, K. G.; Bartolo, D.; Josserand, C.; Bonn, D. Maximum Diameter of Impacting Liquid Droplets. *Physical Review Applied* **2014,** *2* (4), 044018.
5. Mishchenko, L.; Hatton, B.; Bahadur, V.; Taylor, J. A.; Krupenkin, T.; Aizenberg, J. Design of Ice-free Nanostructured Surfaces Based on Repulsion of Impacting Water Droplets. *ACS Nano* **2010,** *4* (12), 7699-7707.
6. Scheller, B. L.; Bousfield, D. W. Newtonian drop impact with a solid surface. *AIChE Journal* **1995,** *41* (6), 1357-1367.
7. Clanet, C.; BÉGuin, C.; Richard, D.; QuÉRÉ, D. Maximal deformation of an impacting drop. *Journal of Fluid Mechanics* **2004,** *517*, 199-208.
8. Bayer, I. S.; Megaridis, C. M. Contact angle dynamics in droplets impacting on flat surfaces with different wetting characteristics. *Journal of Fluid Mechanics* **2006,** *558*, 415-449.
9. Seo, J.; Lee, J. S.; Kim, H. Y.; Yoon, S. S. Empirical model for the maximum spreading diameter of low-viscosity droplets on a dry wall. *Experimental Thermal and Fluid Science* **2015,** *61*, 121-129.
10. Lee, J. B.; Derome, D.; Guyer, R.; Carmeliet, J. Modeling the Maximum Spreading of Liquid Droplets Impacting Wetting and Nonwetting Surfaces. *Langmuir* **2016,** *32* (5), 1299-1308.
11. Lee, J. B.; Laan, N.; de Bruin, K. G.; Skantzaris, G.; Shahidzadeh, N.; Derome, D.; Carmeliet, J.; Bonn, D. Universal rescaling of drop impact on smooth and rough surfaces. *Journal of Fluid Mechanics* **2016,** *786*, 11.
12. Roisman, I. V.; Berberovic, E.; Tropea, C. Inertia dominated drop collisions. I. On the universal flow in the lamella. *Phys. Fluids* **2009,** *21* (5), 10.
13. Roisman, I. V. Inertia dominated drop collisions. II. An analytical solution of the Navier-Stokes equations for a spreading viscous film. *Phys. Fluids* **2009,** *21* (5), 11.
14. PasandidehFard, M.; Qiao, Y. M.; Chandra, S.; Mostaghimi, J. Capillary effects during droplet impact on a solid surface. *Phys. Fluids* **1996,** *8* (3), 650-659.
15. Ukiwe, C.; Kwok, D. Y. On the Maximum Spreading Diameter of Impacting Droplets on Well-Prepared Solid Surfaces. *Langmuir* **2005,** *21* (2), 666-673.
16. Wildeman, S.; Visser, C. W.; Sun, C.; Lohse, D. On the spreading of impacting drops. *Journal of Fluid Mechanics* **2016,** *805*, 636-655.
17. Villermaux, E.; Bossa, B. Drop fragmentation on impact. *Journal of Fluid Mechanics* **2011,** *668*, 412-435.
18. Richard, D.; Quéré, D. Bouncing water drops. *Europhys. Lett.* **2000,** *50* (6), 769-775.
19. Okumura, K.; Chevy, F.; Richard, D.; Quéré, D.; Clanet, C. Water spring: A model for bouncing drops. *Europhysics Letters (EPL)* **2003,** *62* (2), 237-243.
20. Qin, M.; Tang, C.; Tong, S.; Zhang, P.; Huang, Z. On the role of liquid viscosity in affecting droplet spreading on a smooth solid surface. *International Journal of Multiphase Flow* **2019,** *117*, 53-63.
21. Thoroddsen, S. T.; Takehara, K.; Etoh, T. G. Bubble entrapment through topological change. *Phys. Fluids* **2010,** *22* (5), 4.
22. Xu, L.; Zhang, W. W.; Nagel, S. R. Drop splashing on a dry smooth surface. *Physical Review Letters* **2005,** *94* (18), 4.
23. Latka, A. Thin-sheet creation and threshold pressures in drop splashing. *Soft Matter* **2017,** *13* (4), 740-747.
24. Kolinski, J. M.; Mahadevan, L.; Rubinstein, S. M. Lift-Off Instability During the Impact of a Drop on a Solid Surface. *Physical Review Letters* **2014,** *112* (13), 134501.
25. Unverdi, S. O.; Tryggvason, G. A front-tracking method for viscous, incompressible, multi-fluid flows. *Journal of Computational Physics* **1992,** *100* (1), 25-37.
26. Nobari, M.; Jan, Y. J.; Tryggvason, G. Head-on collision of drops—A numerical investigation. *Phys. Fluids* **1996,** *8* (1), 29-42.
27. Tryggvason, G.; Bunner, B.; Esmaeeli, A.; Juric, D.; Al-Rawahi, N.; Tauber, W.; Han, J.; Nas, S.; Jan, Y. J. A Front-Tracking Method for the Computations of Multiphase Flow. *Journal of Computational Physics* **2001,** *169* (2), 708-759.
28. Zhang, Z.; Zhang, P. Kinetic energy recovery and interface hysteresis of bouncing droplets after inelastic head-on collision. *Phys. Fluids* **2017,** *29* (10), 103306.
29. Pan, K.-L.; Law, C. K.; Zhou, B. Experimental and mechanistic description of merging and bouncing in head-on binary droplet collision. *Journal of Applied Physics* **2008,** *103* (6), 064901.
30. Zhang, Z.; Zhang, P. Modeling kinetic energy dissipation of bouncing droplets for lagrangian simulation of impinging sprays under high ambient pressures. *Atomization and Sprays* **2018,** *28* (8), 673-694.
31. Tang, C.; Zhang, P.; Law, C. K. Bouncing, coalescence, and separation in head-on collision of unequal-size droplets. *Phys. Fluids* **2012,** *24* (2), 695.
32. Qian, J.; Law, C. Regimes of coalescence and separation in droplet collision. *Journal of Fluid Mechanics* **1997,** *331*, 59-80.
33. Eggers, J.; Fontelos, M. A.; Josserand, C.; Zaleski, S. Drop dynamics after impact on a solid wall: Theory and simulations. *Phys. Fluids* **2010,** *22* (6), 13.

Figures and captions

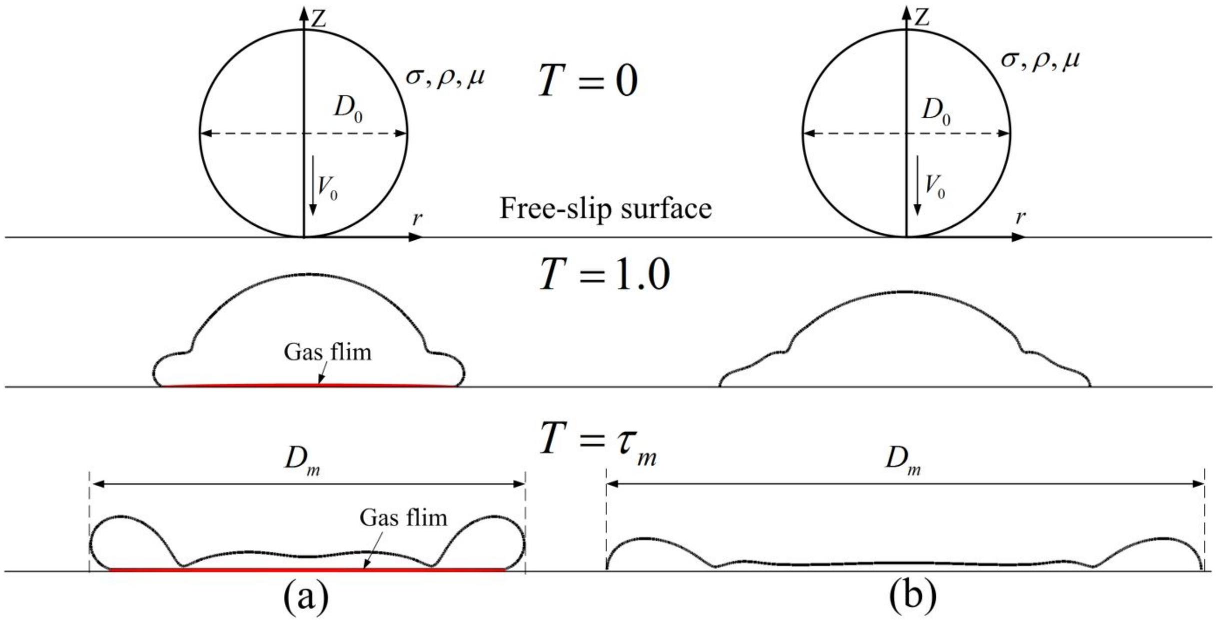

Figure 1. Schematic of droplet impact on a free-slip furface (i.e. a symmetrical plane) (a) with a gas film and (b) without a gas film.

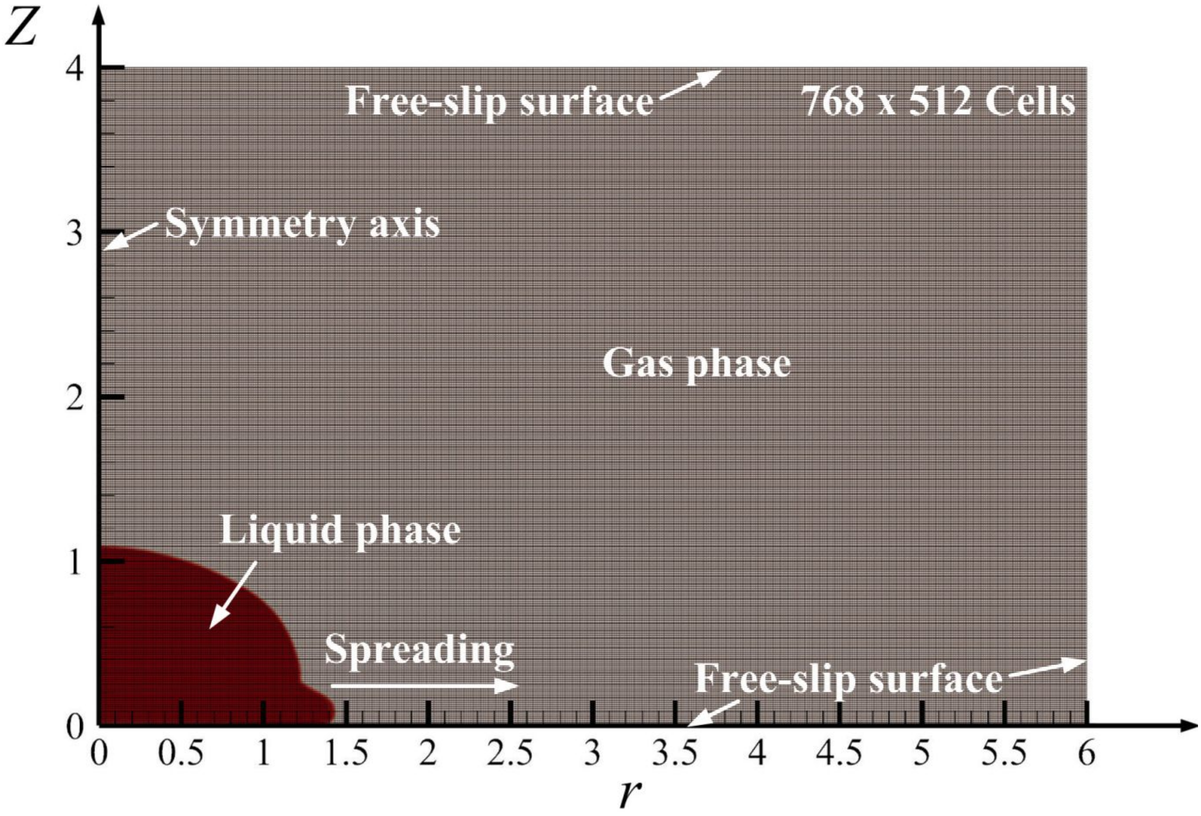

Figure 2. Axisymmetric computational domain with uniform structured grids and specified boundary conditions. Length scales are non-dimensionalized by the droplet radius $R_0 = D_0/2$. Each unit length contains 128 cells.

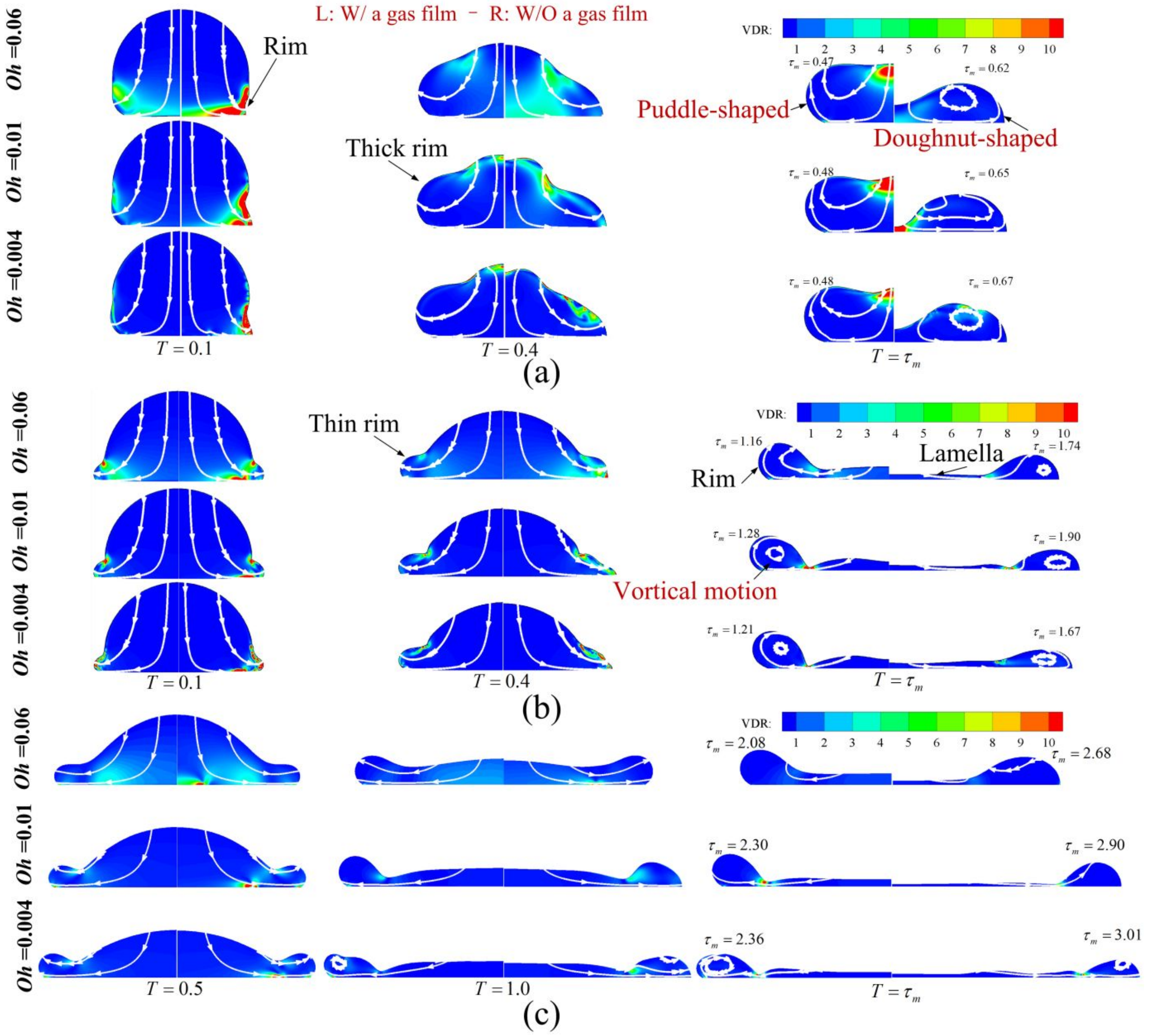

Figure 3. Time sequence of droplet deformation and viscous dissipation of internal flow under three different Ohnesorge numbers Oh for (a) $We_r = 0.25$, (b) $We_r = 2.5$ and (c) $We_r = 5.0$. In each graph, droplet impacting with a gas film is shown on the left half while impacting without a gas film is shown on the right half, strain lines are indicated in each graphs.

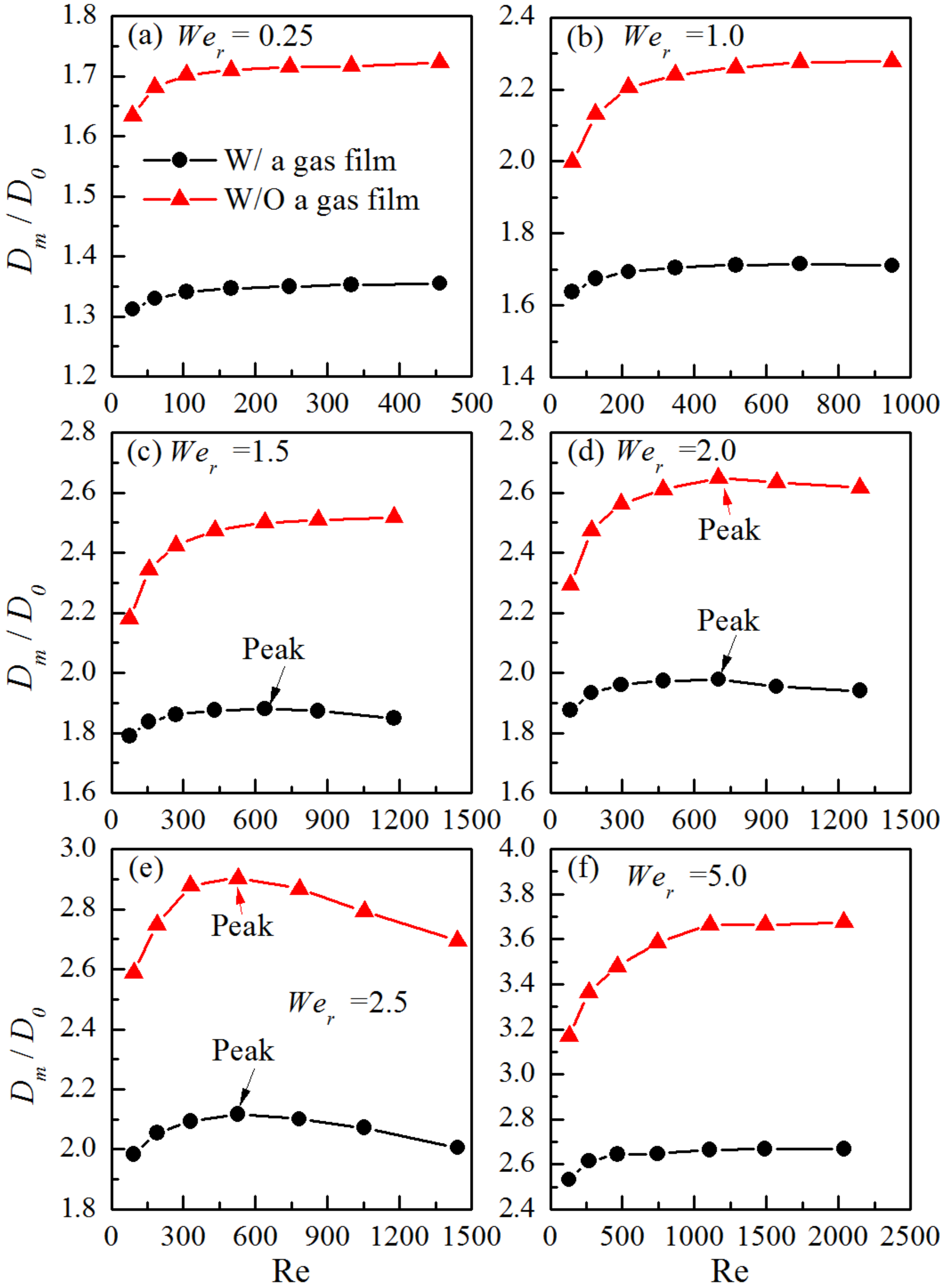

Figure 4. Variation of the maximum spreading of impacting droplet with Re at (a) We_r = 0.25, (b) We_r = 1.0, (c) We_r = 1.5, (d) We_r = 2.0, (e) We_r = 2.5 and (f) We_r = 5.0.

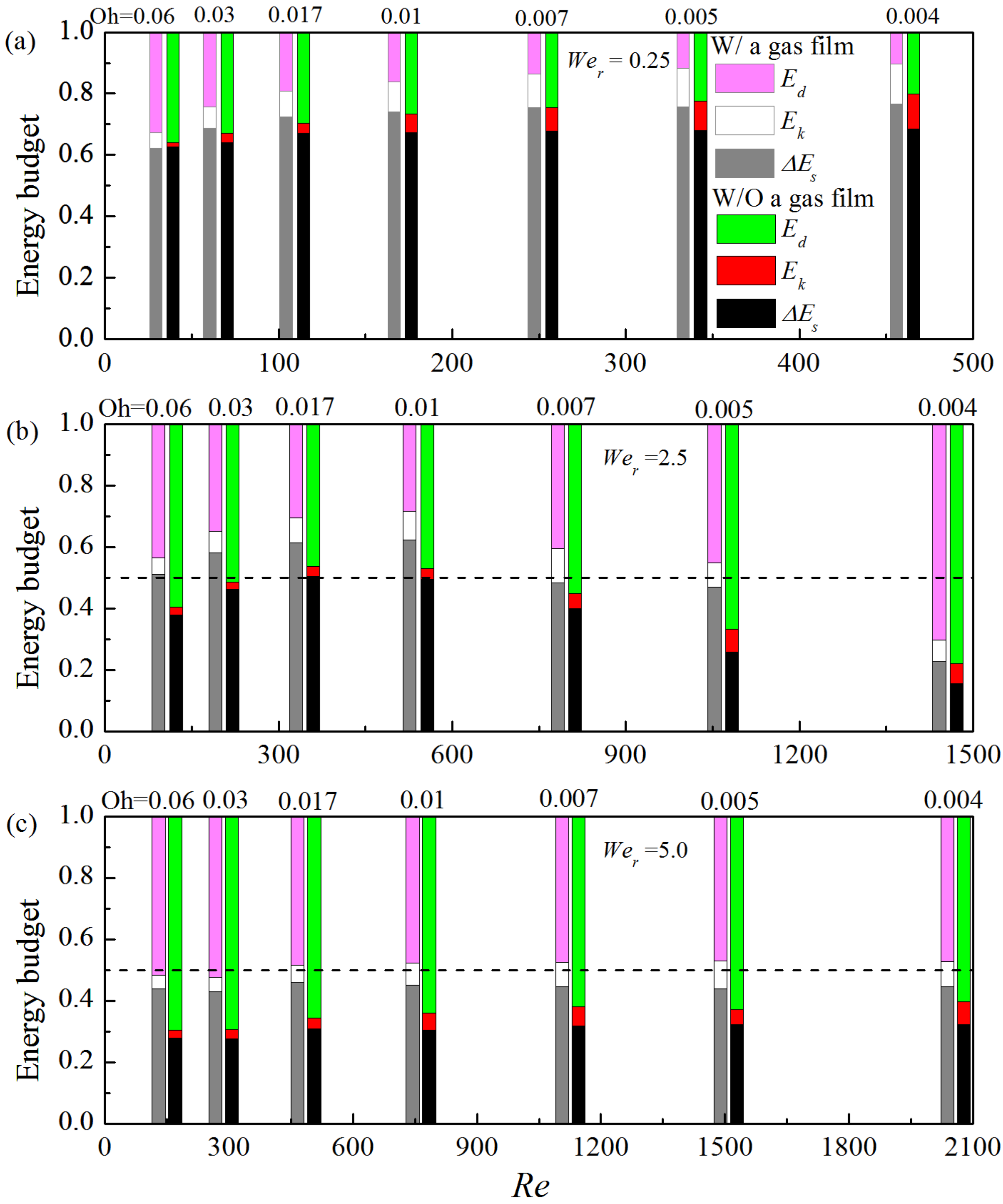

Figure 5. Dependence of energy budget at maximum droplet spreading on Re (or Oh) at (a) $We_r = 0.25$, (b) $We_r = 2.5$, and (c) $We_r = 5.0$. E_d denotes the dissipated kinetic energy, ΔE_s denotes the amount of kinetic energy transferred into the surface energy, and E_k denotes the kinetic energy. The dash lines indicate the "1/2 rule".

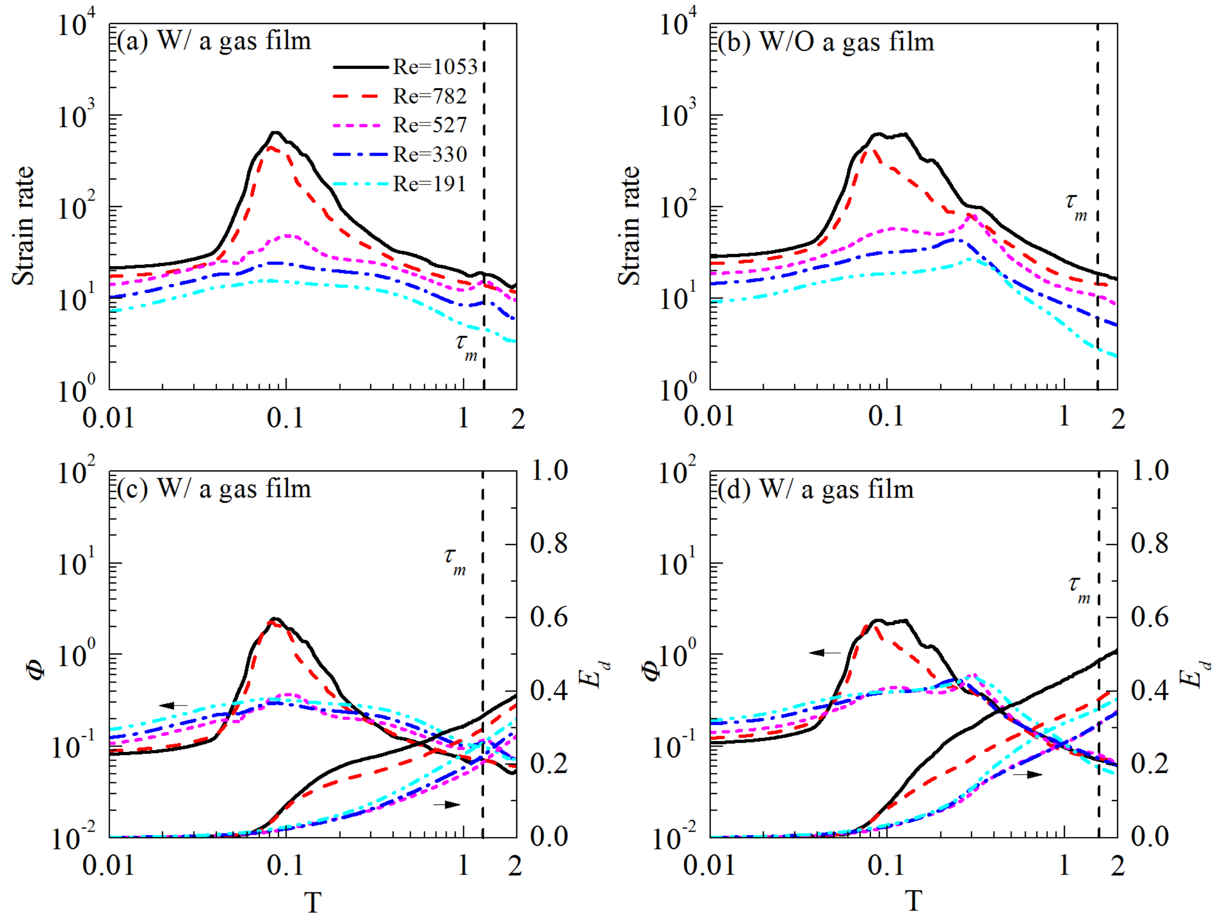

Figure 6. Time evolutions of the strain rate, viscous dissipation rate, and dissipated energy at $We_r = 2.5$ for the cases (a) & (c) with a gas film and (b)& (d) without a gas film.

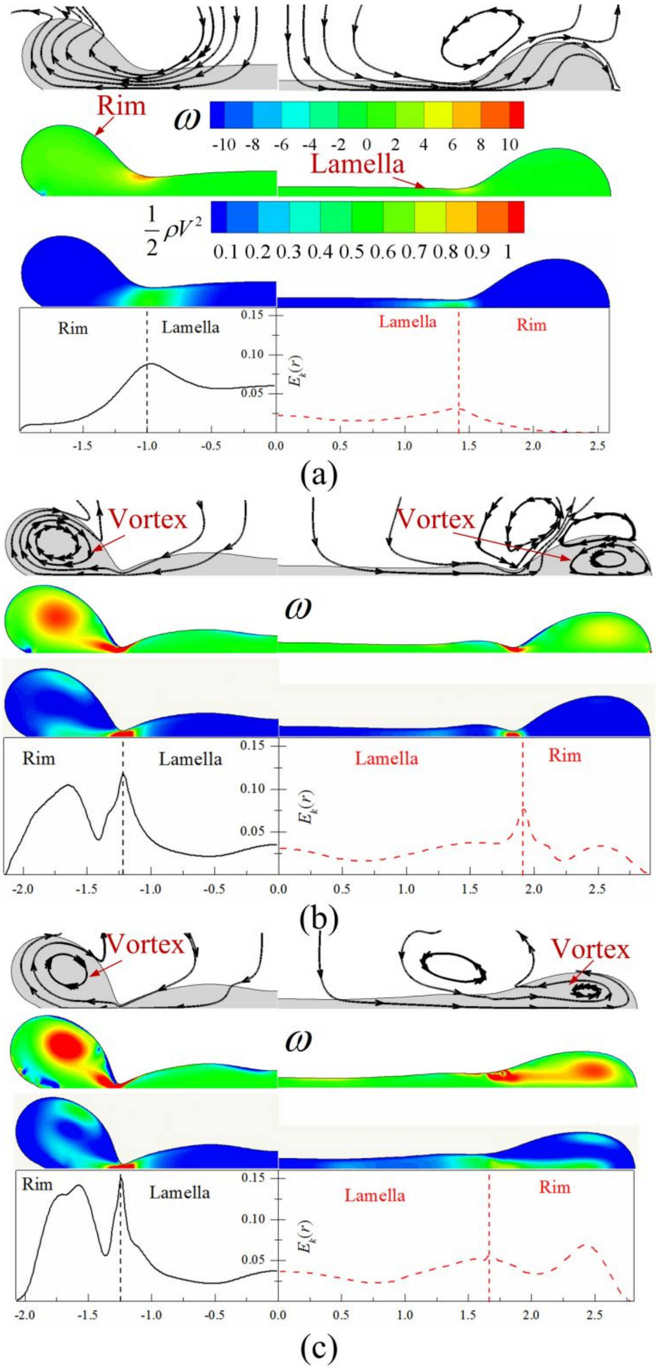

Figure 7. Internal flow, vorticity, and left-over kentic energy distributions at the maximum spreading time τ_m for the cases with a gas film (on the left) and without a gas film at We_r = 2.5 and (a) $Re = 93$ $(Oh = 0.06)$, (b) $Re = 527$ $(Oh = 0.01)$, and (c) $Re = 1053$ $(Oh = 0.005)$.